JACS
JOURNAL OF THE AMERICAN CHEMICAL SOCIETY

Article

pubs.acs.org/JACS

Synthetic Principles Directing Charge Transport in Low-Band-Gap Dithienosilole–Benzothiadiazole Copolymers

Pierre M. Beaujuge,[†,⊥] Hoi Nok Tsao,[‡] Michael Ryan Hansen,[‡] Chad M. Amb,[†] Chad Risko,[∥] Jegadesan Subbiah,[§] Kaushik Roy Choudhury,[§] Alexei Mavrinskiy,[‡] Wojciech Pisula,[‡] Jean-Luc Brédas,[∥] Franky So,[§] Klaus Müllen,[‡] and John R. Reynolds*[,†,∥]

[†]The George and Josephine Butler Polymer Research Laboratory, Center for Macromolecular Science and Engineering, Department of Chemistry, University of Florida, Gainesville, Florida 32611, United States

[‡]Max Planck Institute for Polymer Research, Ackermannweg 10, D-55128 Mainz, Germany

[§]Department of Materials Science and Engineering, University of Florida, Gainesville, Florida 32611, United States

[∥]Center for Organic Photonics and Electronics and School of Chemistry and Biochemistry, Georgia Institute of Technology, Atlanta, Georgia 30332, United States

[⊥]King Abdullah University of Science and Technology (KAUST), Thuwal 23955-6900, Saudi Arabia

Supporting Information

ABSTRACT: Given the fundamental differences in carrier generation and device operation in organic thin-film transistors (OTFTs) and organic photovoltaic (OPV) devices, the material design principles to apply may be expected to differ. In this respect, designing organic semiconductors that perform effectively in multiple device configurations remains a challenge. Following "donor–acceptor" principles, we designed and synthesized an analogous series of solution-processable π-conjugated polymers that combine the electron-rich dithienosilole (DTS) moiety, unsubstituted thiophene spacers, and the electron-deficient core 2,1,3-benzothiadiazole (BTD). Insights into backbone geometry and wave function delocalization as a function of molecular structure are provided by density functional theory (DFT) calculations at the B3LYP/6-31G(d,p) level. Using a combination of X-ray techniques (2D-WAXS and XRD) supported by solid-state NMR (SS-NMR) and atomic force microscopy (AFM), we demonstrate fundamental correlations between the polymer repeat-unit structure, molecular weight distribution, nature of the solubilizing side-chains appended to the backbones, and extent of structural order attainable in p-channel OTFTs. In particular, it is shown that the degree of microstructural order achievable in the self-assembled organic semiconductors increases largely with (i) increasing molecular weight and (ii) appropriate solubilizing-group substitution. The corresponding field-effect hole mobilities are enhanced by several orders of magnitude, reaching up to 0.1 $cm^2 V^{-1} s^{-1}$ with the highest molecular weight fraction of the branched alkyl-substituted polymer derivative in this series. This trend is reflected in conventional bulk-heterojunction OPV devices using $PC_{71}BM$, whereby the active layers exhibit space-charge-limited (SCL) hole mobilities approaching 10^{-3} $cm^2 V^{-1} s^{-1}$, and yield improved power conversion efficiencies on the order of 4.6% under AM1.5G solar illumination. Beyond structure–performance correlations, we observe a large dependence of the ionization potentials of the polymers estimated by electrochemical methods on polymer packing, and expect that these empirical results may have important consequences on future material study and device applications.

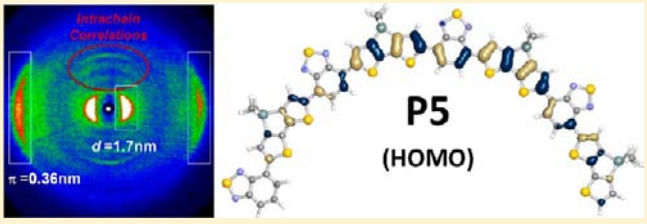

INTRODUCTION

While π-conjugated semiconductors are finding widespread application in a broad range of operating systems, such as thin-film transistors (OTFTs),[1] sensors,[2] photovoltaic devices (OPVs),[3] electrochromic displays,[4] or light-emitting diodes (OLEDs),[5] material performance and charge-transport requirements can vary substantially from one operating system to another. For example, while most existing organic semiconductors with substantial efficiencies in photovoltaic devices do not necessarily fulfill the charge-carrier mobility requirements for thin-film transistor applications, those with packing-dominated charge-transport characteristics may not induce the most favorable morphologies in bulk-heterojunction (BHJ) solar cell devices. In general, organic semiconductors designed for a specific device application tend to not be sufficiently effective in other device configurations.

An excellent illustration of the complexity encountered in attempting to combine (i) solution processability, (ii) high charge-carrier mobilities, (iii) wide-ranging optical absorption profiles and large absorption coefficients, (iv) appropriate energy band structure, and (v) environmental stability with the

Received: February 26, 2012
Published: May 18, 2012

   dx.doi.org/10.1021/ja301898h | J. Am. Chem. Soc. 2012, 134, 8944–8957

same material is represented by the thieno[3,2-b]thiophene-based all-donor polymer analogues developed by McCulloch et al. and others,[6] namely, poly(2,5-bis(3-alkylthiophen-2-yl)-thieno[3,2-b]thiophene)s (PBTTT) (Chart 1). With field-effect hole mobilities as high as 0.6 $cm^2\ V^{-1}\ s^{-1}$ and current on/off ratios on the order of 10^7 in bottom-gate/bottom-contact transistor configurations, PBTTTs stand out as p-channel semiconductors when processed from their mesophase. This level of performance (carrier mobilities approaching that of amorphous silicon) can be obtained under controlled thermal annealing conditions inducing the formation of large crystalline domains[6,7] with nanometer-scale substructures (of ca. 10 nm)[7c] that translate into a high level of microstructural organization. At the same time, in spite of their semicrystalline character, PBTTTs have been shown to possess limited power conversion efficiencies on the order of 2.3% in BHJ solar cells when blended with $PC_{61}BM$.[8] Differences between the in-plane and out-of-plane charge-carrier mobilities are commonly held responsible for photovoltaic performance limitations. These differences are typically attributed to a large extent of edge-on molecular alignment expected to reduce the dimensionality of charge transport across the active layer in highly crystalline semiconducting polymers. Another limiting factor is represented by the lack of spectral coverage, as in PBTTT, for which the onset of absorption lies in the 650−680 nm range while its spectral absorption peaks at ca. 540 nm. The capture of light is in turn restricted to the most energetic photons as opposed to being extended to where the photon flux is maximum (i.e., beyond 600 nm), thus minimizing the external quantum efficiency (EQE) at longer wavelengths. Along these lines, it is worth noting that PBTTT possesses a substitution pattern of solubilizing side-chains, allowing size-controlled intercalation of fullerenes.[9] Besides its plausible consequences on polymer backbone organization, the intercalation of nanometer-sized molecular objects is suspected to govern the optimized composition of the photovoltaic blend, generally toward higher concentration of fullerene,[9] hence possibly disfavoring the light-harvesting capability of the blend. A last critical parameter limiting solar cell performance could be its small ionization potential (IP, 5.1 eV relative to vacuum), inherent to most all-thienylene conjugated polymers, which contributes to minimizing the device open-circuit voltage (V_{OC}) and in turn further limits solar cell efficiency. Overall, as long as a substantial optical density for photovoltaic blends can be extended to longer wavelengths and maintained over a broad spectral range, improving the charge dynamics, including carrier mobilities, achieved with polymers in thin films could enhance both their OTFT and OPV performance.

In recent years, low-band-gap polymers with alternating electron-rich and electron-deficient building units along the same backbone (hence following principles introduced earlier by Havinga and co-workers)[10] have become especially useful in both thin-film transistors and BHJ photovoltaic devices with fullerenes. These polymers provide the ability to span the optical absorption spectrum across the visible and into the near-IR, and improved stability to ambient electrochemical oxidative processes as larger IPs (i.e., low-lying "HOMO" energy levels) can be introduced in conjunction with larger electron affinities (EAs) (i.e., low-lying "LUMO" energy levels). Among these, a poly(diketopyrrolopyrrole-terthiophene) (PDPP3T)[11] with alternating electron-deficient diketopyrrolopyrrole cores and electron-rich unsubstituted thiophenes (Chart 1) demonstrates near-balanced hole and electron mobilities on the order of 10^{-2} $cm^2\ V^{-1}\ s^{-1}$ in bottom-gate/bottom-contact OTFTs. At the same time, PDPP3T exhibits a photoresponse that extends into the near-IR wavelengths (absorption onset at ca. 900 nm), providing for short-circuit current densities on the order of 12 mA cm^{-2} and power conversion efficiencies over 4.5% in BHJ

Chart 1. Molecular Structures of PBTTT and PDPP3T

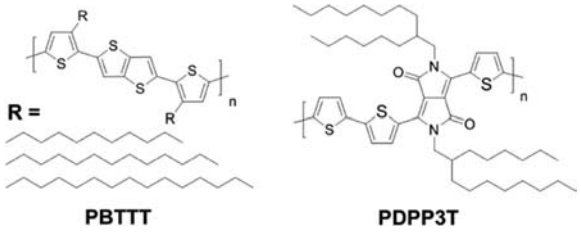

Chart 2. Design Principles Used for the Synthesis of P1−P5[a]

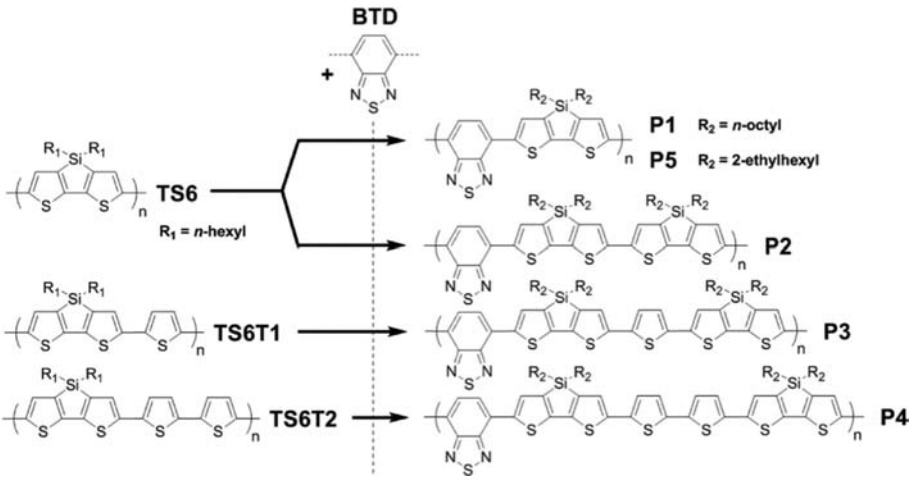

[a]On the left: the all-donor **TS6**, **TS6T1**, and **TS6T2** as originally developed by Marks and co-workers for OTFT applications.[13] On the right: derivatization of the **TS6** backbones with the electron-deficient 2,1,3-benzothiadiazole (BTD) unit to lead to donor−acceptor repeat unit structures narrowing the polymer optical gap.

dx.doi.org/10.1021/ja301898h | J. Am. Chem. Soc. 2012, 134, 8944−8957

Table 1. GPC Estimated Molecular Weights of the DTS-BTD Copolymers P1−P5 (from TCB), TGA-Estimated Decomposition Temperatures (°C), Local Absorption Maxima for the Polymers (in toluene solution and in thin films), and π-Stacking (π, nm) and Chain-to-Chain Lamellar Distances (d, nm) by 2D-WAXS

	M_n (kDa) (PDI)		λ_{abs} (nm) in toluene		λ_{abs} (nm) thin film		2D-WAXS	
polymer	TCB	T_d (°C)	1	2	1	2	π (nm)	d (nm)
P1.1	10.3 (3.6)	422	392	577	404	583	n/a	1.95
P1.2	12.7 (6.3)		408	653 (770)[a]	425	672 (770)[a]	0.35	1.80
P2.1	18.3 (6.1)	429 (312)[b]	458	627	459	643	0.36	(1.95/1.87[c])
P2.2	36.1 (6.0)		469	680	462	653	0.36	1.75
P3	16.3 (8.2)	424	451	602	464	611	n/a	1.94
P4	16.0 (8.0)	426	~480	617	483	645	0.36	1.84
P5.1	18.3 (3.3)		429	703 (764)[a]	427	697 (764)[a]	0.36	1.70
P5.2	26.4 (6.5)		429	703 (764)[a]	427	697 (764)[a]		

[a]Shoulder. [b]Unexpected signature for early degradation. [c]Fiber was annealed at 200 °C for 40 min.

solar cells.[11] PDPP3T and analogues[12] that combine substantial transistor mobilities and solar cell efficiencies suggest that polymer thin-film device performance could be improved by building a more fundamental understanding of the complex interplay between molecular structure and intrinsic charge-transport properties in donor−acceptor systems.

With the goal to identify synthetic principles that impart particularly large carrier mobilities in narrow band gap semiconducting polymers, we designed a series of π-conjugated systems (**P1−P5,** Chart 2) that incorporate distinct ratios of electron-rich to electron-deficient moieties in the monomer repeat unit, along with variations (i.e., concentration and bulkiness) of the solubilizing side-chains along the backbones. **P1−P5** contain a combination of electron-rich substituents examined earlier by Marks and co-workers in OTFTs[13] composed of dithienosilole (DTS) and unsubstituted thiophene spacers. This backbone of electron-rich units was modified by incorporating the electron-deficient core 2,1,3-benzothiadiazole (BTD) in order to (i) study the effect of the donor−acceptor motif on intrinsic charge transport, and (ii) narrow significantly the optical gap of the corresponding polymers, in turn shifting their absorption spectra toward longer wavelengths.

In this contribution, we correlate structural variations imparted to the polymer backbones with their charge-transport properties in thin films, using OTFT and OPV devices as platforms for the study. In particular, using a conjunction of X-ray techniques (2D-WAXS and XRD) supported by solid-state NMR (SS-NMR) and atomic force microscopy (AFM), we emphasize the key role of molecular weight distribution, and the nature of the solubilizing substituents appended to the backbones on the degree of microstructural organization that can be attained with each polymer. While these variables add a higher level of complexity to the equation of design principles governing the performance of polymers in devices, it is increasingly apparent that small structural changes can have a tremendous impact on both charge transport and photovoltaic properties in thin-film devices.[14] Of all the DTS-BTD backbones explored, the highest molecular weight fraction (**P5.2**) of the strictly alternating donor−acceptor derivative **P5** functionalized with 2-ethylhexyl branched substituents stands out by demonstrating up to 0.1 $cm^2\ V^{-1}\ s^{-1}$ field-effect (hole) mobility in bottom-gate/bottom-contact transistors, and by approaching 10^{-3} $cm^2\ V^{-1}\ s^{-1}$ space-charge-limited (SCL) hole mobility in hole-only devices composed of a BHJ of the polymer with the electron-acceptor $PC_{71}BM$. It is essential to note that, in this study, *control* solar cell devices were used as a means of developing fundamental understanding of the correlation between charge transport and OPV efficiency. Knowing the optimized polymer/PCBM blend ratio for each polymer derivative was instrumental to measuring the SCL hole mobilities in hole-only devices composed of a BHJ of the corresponding donors and acceptor. The control solar cells showed PCEs on the order of 4.6% in the absence of small molecule additive-assisted device processing (i.e., no morphology control); this value is in excellent agreement with that previously reported for the same polymer (i.e., 4.7% in average),[14a,15] and approaching the NREL-certified efficiency of ca. 5.2% recently reported using an inverted OPV device configuration.[3d,14b,16]

RESULTS AND DISCUSSION

Polymer Synthesis. The sequence of Pd-mediated Stille couplings used to access the polymers **P1−P5** is shown in Scheme S1, along with a detailed description of our synthetic protocols (see the Supporting Information).

Table 1 shows the number-average molecular weights as determined by high temperature GPC (using trichlorobenzene (TCB) as eluent), the temperatures where the onset of thermal decomposition occurs as determined by TGA (under N_2), and the local absorption maxima in thin film and solution (toluene) for various batches of **P1−P5**. These polymers exhibit excellent thermal stability as evidenced by decomposition temperatures on the order of 400 °C (except for an early sign of degradation at ca. 300 °C in the case of **P2**). Noticeably, two substantial polymer fractions could be isolated by Soxhlet extraction for all of the polymers produced (except for **P3** and **P4**, inherently limited by solubility): a low molecular weight fraction soluble in chloroform (PX.1) and a high molecular weight fraction only soluble in hot chlorobenzene (PX.2). These fractions yield various degrees of structural order and distinct device performance, results that will be discussed in the subsequent sections.

Fiber 2D X-ray Scattering Analysis. The bulk microstructural organization of the polymers was examined by 2D wide-angle X-ray scattering analysis (2D-WAXS) from extruded fibers obtained following previously reported methods.[17] In earlier work,[14c] we showed how small structural changes imparted to the polymer repeat unit on going from **P1.1**, to **P2.1**, to **P3**, and to **P4** affect the degree of microstructural order achievable in the bulk and in thin films of the respective semiconducting polymers. The extent of "crystallinity" of each polymer analogue was further correlated to their performance in thin-film transistors where a trend involving variables such as

the relative concentration of electron-donating and -accepting units along the backbone, or the extent of appended solubilizing side-chains, arose across the series. Here, we further underscore the key role of molecular weight distribution, along with that of the nature of the solubilizing substituents (linear vs branched), on the extent of achievable microstructural organization in DTS-BTD donor–acceptor systems.

Figures 1 and 2 (along with Figure S1) overview the 2D-WAXS patterns obtained for **P1**–**P5** as a function of their

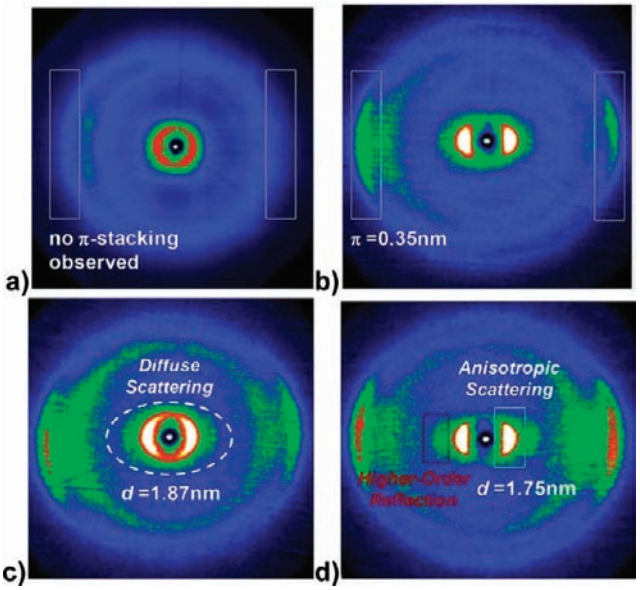

Figure 1. Fiber 2D wide-angle X-ray scattering (2D-WAXS) of (a) **P1.1** (extruded at 170 °C), (b) **P1.2** (extruded at 170 °C), (c) **P2.1** (extruded at 170 °C and annealed at 200 °C), and (d) **P2.2** (extruded at 190 °C).

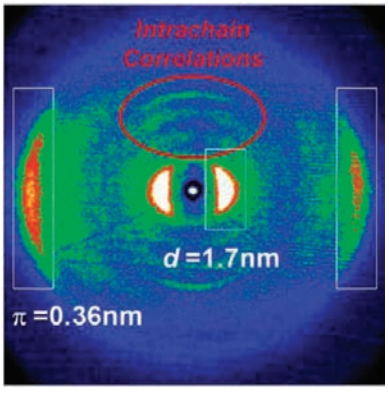

Figure 2. Fiber 2D wide-angle X-ray scattering (2D-WAXS) of **P5.1** (extruded at 210 °C).

repeat unit structure, their molecular weight distribution, or as a function of the postextrusion thermal annealing condition subjected to the fiber (Figure S1), and highlight the differences in attainable structural order across the polymer series. The X-ray data, including π-stacking distances (when observable) and interlamellar spacings, are summarized in Table 1.

In general, looking at the small angle scattering regions, **P1**–**P5** are prone to assemble in lamellar superstructures preferentially oriented in the extrusion direction, as evidenced by the equatorial nature of the Bragg reflections observed along the Debye rings in the most ordered patterns (e.g., Figure 1b and d). For the same reason, examining the wide angle scattering regions, the lamellae show a strong propensity to π-stack in a plane normal to the extrusion direction, rather than along the fiber as is typically seen with small molecular weight discotics forming columnar assemblies (and scattering in the meridional direction).

Figure 1a and b shows the differences in ordering behavior between two molecular weight fractions of the strictly alternating copolymer **P1**, namely, **P1.1** (M_n = 10.3 kDa in TCB) and **P1.2** (M_n = 12.7 kDa in TCB). Here, the first striking indication of a pronounced effect of molecular weight on the degree of observable structural order in the bulk is the clear apparition of wide-angle reflections characteristic of interchain π-stacking interactions (ca. 3.5 Å) on going from **P1.1** to **P1.2**. These reflections are not as pronounced in intensity as those seen in the patterns of **P2.1** and **P4** (see Figure S1), which could be a simple consequence of the molecular weight limitation. In addition, the disruption of isotropy along the smaller-angle Debye rings translates well into a net increase in orientation between lamellae, and is accompanied by a reduction of the *d*-spacing by 1.5 Å (varying from 1.95 to 1.80 nm).

The same decrease in lamellar distance is also illustrated in Figure 1c and d comparing two distinct molecular weight fractions of polymer **P2**, namely, **P2.1** (M_n = 18.3 kDa in TCB) and **P2.2** (M_n = 36.1 kDa in TCB). In this case, while the short π-stacking distance of 3.6 Å is retained from one batch to the other (and regardless of the extrusion conditions and thermal annealing subjected to the fiber), the lamellar spacing dropped from 1.87 to 1.75 nm. Visible in Figure 1d, the presence of a higher-order anisotropic reflection at small angles is additional evidence for the even more pronounced molecular-weight-promoted ordering effect in **P2** in comparison to **P1**. Moreover, a significant distinction between **P2** and **P1** is represented by the higher intensity π-stacking reflections of **P2**, which further translates into a larger degree of relative chain-to-chain order.

Variations in microstructural organization with molecular weight are expected given that the degree of molecular entropy in conjugated polymers (e.g., entanglement) varies with average chain lengths. As empirically observed in the case of **P1** and **P2**, shorter lamellar distances between backbones can be obtained with higher average molecular weight fractions (see Table 1). This could be explained by considering polymer chain-ends as defects disrupting the self-assembling polymer lattices. Following this reasoning, a lower-molecular-weight polymer fraction contains a higher concentration of distinct chain-ends and necessarily meets inherent limitations in terms of attainable structural order. In contrast, the possibility that the degree of entanglement promotes shorter molecular distances by "tightening" the polymer lattice is not consistent with the higher degree of chain orientation seen with the large molecular weight fractions in general (as clearly evidenced by a diminution of the scattering accounting for the lamellar organization).

Based on solution processability considerations, copolymers **P3** (M_n = 16.3 kDa) and **P4** (M_n = 16.0 kDa) were examined without further attempt to achieve higher molecular-weight fractions. As illustrated in Figure S1e, and in contrast with the higher molecular-weight fractions of **P1** and **P2**, **P3** revealed relatively isotropic diffractions at small angles (*d* = 1.94 nm) with the absence of observable π-stacking at wider angles. In

dx.doi.org/10.1021/ja301898h | J. Am. Chem. Soc. 2012, 134, 8944–8957

comparison, and as shown in Figure S1f, the pattern of **P4** (bithiophene-substituted analogue of **P3**) reveals π-stacking distances as low as 3.6 Å and fewer scattered small-angle reflections, thus supporting a more pronounced relative orientation of the backbones, and narrower lamellar distances on the order of 1.84 nm.

As illustrated in Figure S1a–d, postextrusion thermal annealing of the fibers of **P1.2** and **P2.2** does induce some additional ordering characteristics in the bulk polymers, which is evidenced by the more pronounced π-stacking reflections, though the effect remained relatively modest.

In parallel, comparing the highest molecular weight of **P1** attained, namely, **P1.2**, and its branched 2-ethylhexyl-substituted counterpart **P5.1**, whose X-ray scattering pattern is shown as Figure 2, it appears that side-chain dynamics can further promote the extent of achievable microstructural organization both by imparting proper interchain spacing in the solid state, and by introducing appropriate material solubility. On one hand, in the case of **P5.1**, the bulkier nature of the 2-ethylhexyl substituents (versus the linear octyls) allows a higher degree of polymerization to be attained by preventing premature precipitation during polymerization. As discussed above, longer backbones can induce higher ordering capabilities. On the other hand, and as reported in Table 1, the shorter nature of the hexyl segment in 2-ethylhexyl versus that of a linear octyl (calculated to be shorter by 1.3 Å at the DFT-ωB97XD/6-31G(d,p) level)[18] induces an interlamellar distance of only 1.70 nm, which is significantly shorter than the 1.80 nm spacing measured for the higher molecular weight fraction of **P1** (**P1.2**), and is also the shortest lamellar spacing observed across this polymer series. Nonetheless, the 0.1 Å increase in π-stacking distance on going from **P1.2** to **P5.1**, which could be explained by the presence of the 2-ethyl substituent branching out of the core solubilizing chain, may also be "loosening" the polymeric network and promoting the favorable self-assembly of **P5.1**. In light of these empirical results, 3.5 Å could therefore be interpreted as being a lower threshold for material processing (i.e., closer stacking largely reducing processability) and relatively unhindered nanostructural organization in stackable π-conjugated polymers. Overall, the distinct and particularly favorable ordering behavior of **P5.1** when compared to its linearly substituted counterparts **P1**–**P4** is expected to impact device performance (vide infra).

Solid-State NMR. Insights into the molecular order and local packing arrangement of the DTS-BTD donor–acceptor polymers can tentatively be produced from solid-state NMR by probing the local molecular environments of proton (^{1}H) and carbon (^{13}C) sites reflected in their chemical shift values.[19] The distinction relies on the fact that the packing of self-assembled aromatic-based systems induced by π–π interactions is mainly observed as a nucleus *independent* shift to higher or lower chemical shift on the order of 1–10 ppm as compared to the isotropic chemical shift (δ_{iso}) observed in solution NMR.[20] This makes ^{1}H NMR the obvious choice for probing this type of interaction, since this nucleus has a much *lower* chemical shift dispersion (~15 ppm) as compared to ^{13}C (~220 ppm).[19] The structural order or disorder is, on the other hand, mainly reflected in the line width of the observed isotropic chemical shifts for the different chemical moieties of the probed molecule.[19] For this reason, ^{13}C is a more appropriate method for probing local order since this nucleus has a *larger* chemical shift range leading to a better chemical shift resolution. Moreover, it is not influenced by homonuclear dipole–dipole couplings as in the case of ^{1}H NMR in solids. In fact, the observed line width differences for the isotropic chemical shifts of a number of different NMR active nuclei have been exploited for a large range of compounds. This includes organic and inorganic materials and has led to a better understanding of the short and intermediate range order present in both semicrystalline and amorphous materials.[21] Thus, combining the information available from observing two different nuclei (^{1}H and ^{13}C), using MAS (magic angle spinning) NMR methods,[22] it is possible to get a more detailed picture of both local packing arrangements and molecular order.

Figure 3 shows the solid-state NMR results obtained for the high molecular-weight fraction of the DTS-BTD derivative

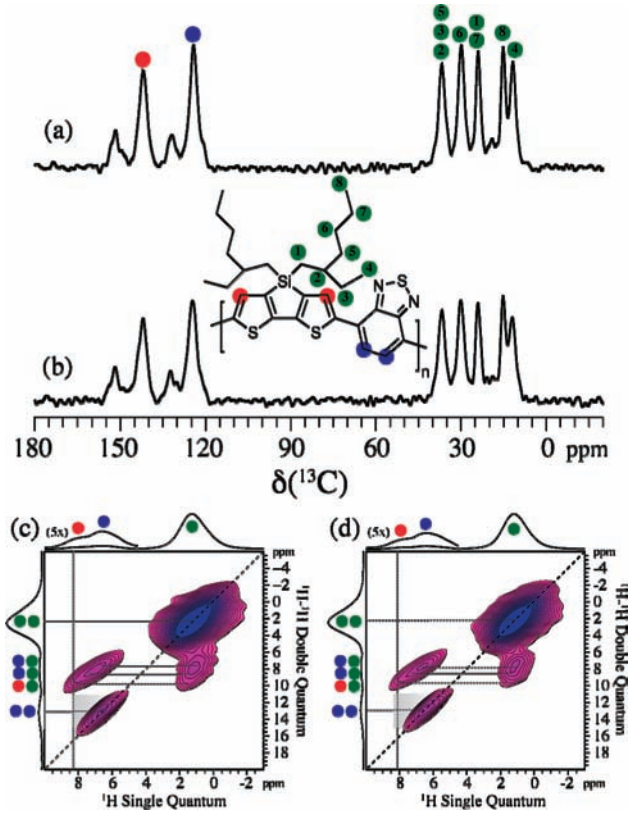

Figure 3. Morphology changes in **P5.2** probed by 2D solid-state ^{1}H–^{1}H DQ-SQ correlation and ^{13}C{^{1}H} MAS NMR after thermal annealing (a, d) and before annealing at 200 °C (15 min) (b, c). A cross-polarization time of 1.0 ms was used for the 1D spectra (a, b), and a back-to-back recoupling and reconversion period of 40 μs was employed for the 2D correlation spectra (c, d). All spectra were recorded at 16.4 T using a fast spinning speed of 50.0 kHz.

P5.2 (26.4 kDa) substituted with 2-ethylhexyl branched solubilizing side chains, before and after sample annealing at 200 °C. Before annealing, the ^{13}C{^{1}H} CP (cross-polarization)/MAS spectrum (Figure 3b and c) exhibits a good resolution in the region characteristic for the side chains (5–45 ppm). After annealing (Figure 3a and d), these resonances are even more resolved (decrease in linewidths of about 40–50 Hz), a result suggesting that improved order of the side chains has been achieved. Upon side-chain reorganization at elevated temperatures, the π-conjugated backbones are expected to rearrange. The 2D ^{1}H–^{1}H DQ-SQ (double quantum–single quantum) correlation spectra shown in Figure 3c and d give some indications on the evolution of the packing of the

dx.doi.org/10.1021/ja301898h | J. Am. Chem. Soc. 2012, 134, 8944–8957

polymer backbone with thermal annealing. Here, improved resolution with thermal annealing is apparent from the off-diagonal cross peaks. These signals originate from the close spatial proximity between the proton sites at the polymer backbone and those of the attached 2-ethylhexyl side chains. The improved ^{1}H resolution is consistent with the better local order observed in the ^{13}C{^{1}H} CP/MAS NMR spectra. Neither of the 2D spectra in Figure 3c and d shows any significant DQ-SQ correlations between DTS and BTD, and DTS and DTS groups. However, the donor−acceptor correlation (DTS-BTD) is observable at longer recoupling time (Figure S2), in agreement with our recent results obtained with an analogous polymer backbone for which the donor units are bridged by a carbon center substituted with linear dodecyl side chains.[23] In Figure 3c and d, the resonance close to the diagonal from the two different BTD protons displays an elongated and slightly split line shape, extending toward lower frequency. These features suggest that the DTS-BTD polymer backbones are indeed π-stacked, but also show that the BTD acceptor units are heterogeneously packed throughout the sample; that is, the acceptor groups are not always located at the exact same position with respect to the neighboring polymer chains. These results suggest that the molecular structure changes induced on the donor, including bridging atom substitution and side-chain substituent variations, are not a critical parameter influencing polymer packing according to SS-NMR. We note that it has been suggested in a recent study that the incorporation of silicon bridging centers on the donor leads to an increase of the angle between donor and acceptor groups, going from 10° in carbon-bridged donor-containing systems to 19° in silicon-bridged donor-containing ones.[14b] This variation in backbone geometry could explain why the appearance of the donor−acceptor correlations are only observed at longer recoupling times (see Figure S2).

In order to identify a possible molecular-weight dependence of π-stacking and lamellar organization, two samples of **P1** with distinct molecular weight distributions were characterized by solid-state NMR (**P1.1**, 10.3 kDa; and **P1.2**, 12.7 kDa). The results from these investigations are summarized in Figure S3 (see the Supporting Information). Important similarities exist among the chemical shifts seen in all ^{13}C{^{1}H} CP/MAS NMR spectra (Figure S3a−d), and only minor improvements in line widths are observed in the region of the side chains after the samples have been annealed. Following the conclusions drawn earlier for **P5**, this provides evidence that thermal annealing affects the reorganization of appended octyl side chains, albeit to a relatively modest extent for the two molecular weight fractions of **P1** shown here. Interestingly, the effect of annealing at 200 °C appears to be less pronounced for **P1** than for **P5**. A possible explanation for this difference could be that the longer octyl side chains introduce more conformational disorder in comparison to the shorter branched 2-ethylhexyl chains of **P5**. In theory, linear octyl side chains can adopt both "linear" (all-trans) and "random coil" (predominant gauche) conformations in the condensed state of the copolymer. In contrast, the shorter branched 2-ethylhexyl pendant chains would be somewhat less flexible, while allowing more interlamellar reorganization (in consistency with the larger π-stacking distance of 3.6 Å estimated for **P5** by 2D-WAXS). In other words, the structural disorder introduced by the linear octyl side chains cannot be easily removed by annealing the sample. Importantly, the 2D ^{1}H−^{1}H DQ-SQ correlation spectrum of **P1.2** (Figure S3e) shows an even more elongated line shape (toward lower frequencies) for the BTD protons in comparison to that observed for **P5.2** (Figure 3b); this result suggests increased nonuniformity of packing of the BTD accepting units in **P2.1** in comparison to **P5.2**. The elongation to higher frequency is most likely due to a DQ-SQ correlation arising from the packing of acceptor-acceptor groups on top of one another.

Polymer Electrochemical Properties. Taking into consideration the range of differences in intrinsic material structural organization properties emphasized above, the thin-film electrochemical properties of **P1**−**P5** were next to be examined with specific attention to the possible interplay between propensity to order and subtle/unexpected variations in redox onsets. The redox properties of **P1**−**P5** were investigated via cyclic voltammetry (CV) and differential pulse voltammetry (DPV) (see Figures S4−S10) with the purpose of correlating the polymer oxidation and reduction potentials and respective electrochemical energy gaps induced by the successive structural modifications to the repeat unit with the theoretical trends predicted at the DFT level. A three-electrode electrochemical cell composed of a platinum disk working electrode (0.02 cm^{2}), a platinum flag counter electrode, and a Ag/Ag^{+} reference electrode (10 mM $AgNO_3$, 0.1 M Bu_4PF_6 in MeCN) was employed, and all results were subsequently calibrated to Fc/Fc^{+} (for consistency with values reported in the literature). The estimated polymer energy levels (IP^{SS} and EA^{SS}) are presented in Table S1 (see the Supporting Information) and provided relative to the vacuum level, considering that the SCE is 4.7 eV versus vacuum[24] and Fc/Fc^{+} is 0.38 eV vs SCE,[25] that is, ∼5.1 eV relative to vacuum. The polymer films were cycled until they reached a stable and reproducible redox response prior to characterization. The respective polymer optical gaps as determined from the onset of their low-energy transition (thin-film value) are also presented in Table S1.

It is worth noting that, while cyclic voltammetry prevails as the most common electrochemical method presented throughout the π-conjugated polymer literature, DPV is now clearly established to allow for higher sensitivity, yielding sharper redox onsets as a result of a reduction of charging currents.[26] This, in turn, increases the accuracy of the energy gaps estimated electrochemically; as such, DPV values will be the primary values referred to throughout this work, while CV values are only reported for comparison with other important contributions on the topic. The benefits of using DPV over CV in this study are illustrated in Figure 4, which overlays the voltammograms obtained via the two approaches. Here, our interpretation of the CV of **P2.2** reveals a difference of 150 mV in the onset of oxidation between the CV and DPV of the same polymer film, with the CV onset being somewhat ambiguous. As an added level of complexity, the various methods of determining electrochemical onsets[27] (e.g., intersecting tangents) can lead to different interpretations of where the onset actually occurs within the range 0.1−0.4 V, whereas DPV provides a sharp onset at which the oxidation is observed at 0.10 V.

In addition to using DPV to determine redox onsets, we found that particularly thin films of polymer drop-cast from dilute solutions (0.1−0.25 mg mL^{-1}) onto platinum disk electrodes from chlorobenzene solutions yielded more electrochemically reversible voltammograms, and narrower electrochemical energy gaps when compared to thicker films deposited from more concentrated casting solutions (see Figures S11−

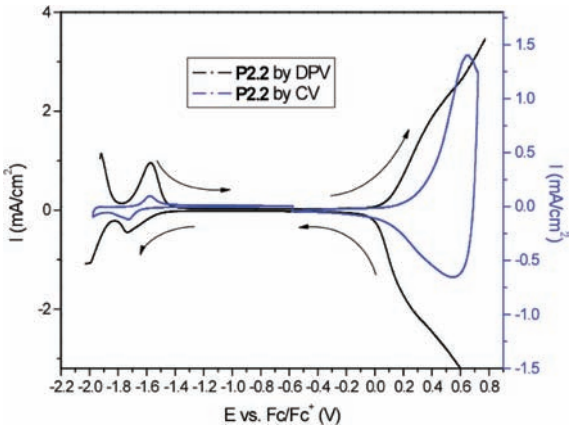

Figure 4. CV (blue curve, 50 mV/s scan rate) and DPV (black curve, step size 2 mV, step time 38 ms, pulse amplitude 100 mV) of a thin film of **P2.2** drop-cast from chlorobenzene on a platinum disk immersed in 0.1 M Bu_4NPF_6/PC solution. Arrows indicate direction of scans.

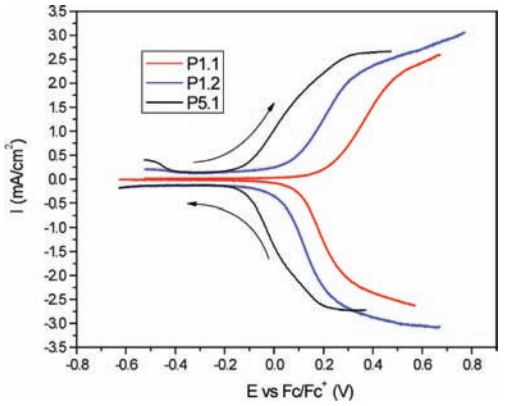

Figure 5. DPV (step size 2 mV, step time 38 ms, pulse amplitude 100 mV) of thin films of **P1.1**, **P1.2**, and **P5.1** drop-cast on a platinum disk electrode immersed in 0.1 M Bu_4NPF_6/PC solution. Arrows indicate scan direction.

S15). This behavior is attributed to the neutral state polymer network being essentially insulating in character, inhibiting ion transport, and increasing uncompensated resistance. The use of thick polymer layers, in essence more polymer on the electrode, is expected to increase resistance and the total amount of charge passing. This induces larger ohmic polarization and thus creates larger overpotentials through the relationship shown in eq 1, whereby the potential of the working electrode E at a certain current flow is equal to the sum of the null potential (E_n), ohmic polarization (or uncompensated resistance, IR_u), activation polarization (η_{act}), and concentration polarization (η_{conc}).[28] Since activation polarization is intrinsic to the analyte at a given interface, and since concentration polarization can be neglected for a film sufficiently thin, employing relatively thin polymer films can be expected to limit polarization effects in general. As a result, the overpotential required for current flow can be minimal, and the same thin films can be used for the measurement of electrochemical onsets close in value to the true thermodynamic potentials.

$$E = E_n + IR_u + \eta_{act} + \eta_{conc} \quad (1)$$

Importantly, as can be seen from Table S1, significant differences in redox potential values arise on going from one conjugated backbone to another, on changing the solubilizing substitution pattern, and depending on the molecular weight fraction considered. In particular, **P1.1**, **P1.2**, and **P5.1** all contain the same conjugated backbone, but the onsets of oxidation differ by 300 mV as evidenced by their respective DPVs shown in Figure 5. In this case, it is interesting to note that decreasing the oxidation potential correlates with increasing the thin-film structural ordering capabilities. In particular, while the lower molecular weight fraction of **P1**, namely, **P1.1**, demonstrated less "crystallinity" than **P1.2** by 2D-WAXS analysis, the oxidation potential of **P1.2** is found to be 140 mV lower than that of **P1.1** (0.22 and 0.08 V, respectively). In comparison, the 2-ethylhexyl-substituted analogue of **P1**, namely, **P5.1**, showing particularly pronounced "crystallinity" from 2D-WAXS with signatures of long-range order, yields the lowest potential of oxidation at −0.12 V versus Fc/Fc^+. It should be noted that this potential is strikingly different from independently reported values estimated by CV (+0.25 V).[15] Here we found that particularly thin films of this polymer need to be analyzed to reveal much lower oxidation potentials by CV (onset around −0.1 V). This result further underscores the greater sensitivity attained in using DPV vs CV when determining electrochemical onsets.

In relating oxidation potentials and thin-film structural ordering capabilities, it is also worth noting that the oxidation potential of **P2.1** is 120 mV higher than that of its higher molecular weight counterpart **P2.2** (0.22 V versus 0.10 V, respectively) while **P2.2** exhibits more "crystallinity" in 2D-WAXS measurements.

In contrast, the reduction potentials of all the polymers were nearly identical as measured by CV and DPV, yielding onset values on the order of −1.6 and −1.5 V versus Fc/Fc^+, suggestive of a polymer reduction potential governed by the reduction of the electron-deficient BTD units. In addition, for all polymers except **P1.2**, the peak reductive current (as measured by CV) either remained the same or decreased upon increasing film thickness (see Table S2), suggesting that the negative charge injected into the polymers was not mobile throughout the bulk material. This assertion is supported by the FET charge transport study (vide infra), whereby no evidence for n-type transport was observed in any of the polymers in combination with the dielectrics used in our laboratories. Looking more closely at the DPV results, it seems that the reduction onsets of **P1.1**−**P4** approach −1.5 V, with the exception of that observed for the more ordered system **P5.1** showing a reduction at −1.39 V. Here, it is reasonable to associate the measurement of a lower reduction potential to the more pronounced "crystallinity" in thin films of **P5.1**.

Overall, these results support the idea that redox potentials in π-conjugated polymers are not only governed by the chemical/molecular structure of the repeat units, but also by the distinct microstructural ordering propensities of each system; that is, the final measurable properties are emergent characteristics of the material. This is highlighted by the comparable ionization potentials and electron affinities determined for similarly sized oligomers across the polymer series at the B3LYP/6-31G(d,p) level of theory. Accordingly, in addition to the repeat unit structure parameter, molecular-weight distribution, side-chain concentration, and side-chain structure represent a set of important factors that influence the magnitude of the ionization potentials in the solid-state polymer materials. Of course, the same parameters should also be expected to impact the overall performance of thin-film devices.[6,11,29]

dx.doi.org/10.1021/ja301898h | J. Am. Chem. Soc. 2012, 134, 8944−8957

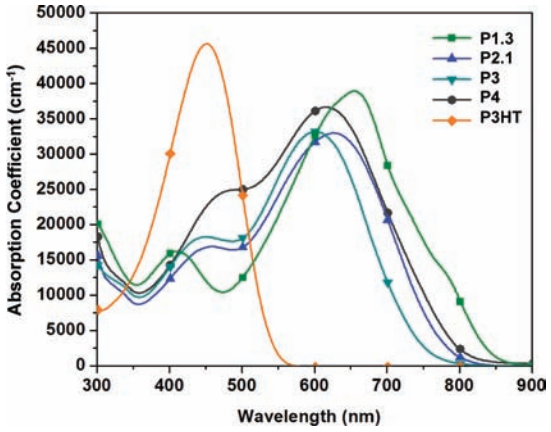

Figure 6. Absorption coefficients as a function of wavelength for **P1**–**P4** (along with those for P3HT). The absorption coefficients (in cm^{-1}) are derived from the mass absorption coefficients (in L g^{-1} cm^{-1}) measured in toluene solution by assuming a density of 1 g cm^{-3} for all polymers. (Figure adapted with permission from ref 4b. Copyright 2010 American Chemical Society.)

Polymer Optical Properties. The absorption spectra of **P1**–**P4** were recorded in toluene solutions and for thin films (see Table 1). In Figure 6, the mass absorption coefficients of **P1**–**P4** (in L g^{-1} cm^{-1}) have been converted to "thin-film" absorption coefficient values (in cm^{-1}) by assuming a density of 1 g cm^{-3} for all polymers (e.g., poly(3-octylthiophene)[30] ~ 1.05 g cm^{-3}).[4b] The UV–visible spectrum of regioregular poly(3-hexylthiophene) (P3HT) is superimposed for comparison.

As expected from previous work investigating the spectral distribution of π-conjugated polymers with intramolecular donor–acceptor interactions,[4b,31] **P1**–**P4** possess a "dual-band" of absorption evolving as a function of the ratio of electron-rich to electron-deficient building units incorporated along the backbone. In comparison with their all-donor π-conjugated parents,[13] the onsets of absorption of **P1**–**P4** are red-shifted by ca. 150 nm toward longer wavelengths, with the smallest optical gap obtained for **P1.2** (1.4 eV), in which the concentration of electron-deficient units along the backbone is the largest across the polymer series. While their maximum of absorption peaks in the range 600–650 nm, the second local maximum located at shorter wavelengths is more sensitive to the concentration of electron-rich units present in the backbone and shifts from ca. 410 nm to ca. 480 nm. Noticeably, the dual-band absorption of **P4** is the most coalesced and balanced of all, while maintaining high absorption coefficients across the visible spectrum.

The empirical trends for the first transition energies are well reproduced by time-dependent density functional theory (TDDFT) calculations at the B3LYP/6-31G(d,p) level; see Tables S1 and S7 (even if the effects of electron self-interaction from the general DFT formalism result in a red shift of the transition energies). The $S_0 \rightarrow S_1$ transitions for **P1**–**P4** are principally described as HOMO→LUMO transitions in the one-electron picture, though other close-lying frontier molecular orbitals (in particular HOMO-1 and LUMO+1) contribute to the description of the excitation.

Overall, **P1**–**P4** absorb more effectively where the solar photon flux is the most intense (that is in the 600–800 nm range) in comparison to their all-donor parents,[13] a result that could promote their efficiency in solar cell devices.

Transistor Fabrication and Characterization. In order to probe the effect of the synthetic modifications made on charge transport, bottom-gate/bottom-contact FET devices were constructed on heavily doped Si wafers covered with 200 nm of thermally grown dielectric SiO_2 passivated with hexamethyldisilazane (HMDS). The gold contact electrodes were patterned using conventional photolithographic methods to yield 50 μm long and 3500 μm wide channels. The semiconducting polymer layers were drop-cast from *o*-dichlorobenzene (2 mg mL^{-1}) onto a hot-plate preheated to 100 °C, or spin-cast from the same solvent, and were subsequently annealed for 15 min at various temperatures (vide infra). The solution-processing of the active layer and device testing were carried out under N_2 atmosphere in a glovebox. Table 2 gives an overview of the field-effect transistor performance obtained across the polymer series, including hole mobility and on/off current ratios, comparing drop-cast and spin-cast processing methods. The molecular weight and 2D-WAXS results described in Table 1 are also reported in Table 2 in order to facilitate drawing direct correlations with the FET mobility results.

The first striking dependence of the electronic device performance on the polymer molecular weight is represented by the higher molecular weight fraction of **P1**, namely **P1.2** (M_n = 12.7 kDa in TCB), raising the FET hole mobility from 2 ×

Table 2. Overview of Field-Effect Transistor Performance Obtained across Polymer Series[a]

	M_n (PDI)	2D-WAXS		FET drop-cast		XRD[drop]			FET spin-cast	
polymer	TCB	π	d	I_{on}:I_{off}	μ_{SAT}	anneal.	d	I_{on}:I_{off}	μ_{SAT}	anneal.
P1.1	10.3 (3.6)	n/a	1.95	1×10^{2}[c]	2×10^{-6}[c]	100				
P1.2	12.7 (6.3)	0.35	1.80	5×10^{3}	1×10^{-2}	150	1.85	3×10^{2}	1×10^{-4}	200
P2.1	18.3 (6.1)	0.36	(1.95/1.87[b])	6×10^{3}	3×10^{-4}	100				
P2.2	36.1 (6.0)	0.36	1.75	2×10^{4}	4×10^{-2}	225	1.79	1×10^{4}	7×10^{-3}	200
P3	16.3 (8.2)	n/a	1.94	2×10^{4}	3×10^{-3}	100	1.99	2×10^{3}	9×10^{-4}	200
				3×10^{5}	1×10^{-2}	175				
P4	16.0 (8.0)	0.36	1.84	1×10^{3}	2×10^{-2}	100	1.83	2×10^{3}	7×10^{-4}	200
				6×10^{4}	5×10^{-2}	250				
P5.1	18.3 (3.3)	0.36	1.70	1×10^{5}	1×10^{-1}	150	1.74	1×10^{4}	5×10^{-3}	200

[a]Number average molecular weight in TCB (M_n, kDa). π-Stacking (π, nm) and chain-to-chain lamellar distances (d, nm) by 2D-WAXS. Charge-carrier mobilities at saturation (μ_{sat}, cm^2 V^{-1} s^{-1}) and current on/off ratios (I_{on}:I_{off}) in drop-cast FETs for copolymers **P1.1**, **P1.2**, **P2.1**, **P2.2**, **P3**, **P4**, and **P5.1** on HMDS-passivated SiO_2. Annealing temperature (°C) for the drop-cast FETs. XRD chain-to-chain distances (d, nm) as measured from the drop-cast FET devices. Charge-carrier mobilities at saturation (μ_{sat}) and current on/off ratios (I_{on}:I_{off}) in spin-cast FETs for copolymers **P1.2**, **P2.2**, **P3**, **P4**, and **P5.1** on HMDS-passivated SiO_2. [b]Fiber was annealed at 200 °C for 40 min. [c]FET made on PTES-passivated SiO_2.

dx.doi.org/10.1021/ja301898h | J. Am. Chem. Soc. 2012, 134, 8944–8957

10^{-6} to 1×10^{-2} cm^2 V^{-1} s^{-1} in a drop-cast transistor processed following the same conditions as those used with **P1.1** (M_n = 10.3 kDa in TCB). The same device showed only a slight increase to 1×10^{-2} cm^2 V^{-1} s^{-1} on annealing at a temperature identified as providing the best device performance for the drop-cast polymer (150 °C here), a result consistent with the modest increase in microstructural order observed in the fiber annealed at elevated temperatures (see Figure S1a and b). This increase by ca. 4 orders of magnitude obtained with **P1.2** is all the more surprising that an average molecular weight difference of less than 3 kDa exists on going from **P1.1** to **P1.2**, but correlates well with the differences observed in the respective X-ray patterns of the two fractions (see Figure 1a and b), and is attributed to the combination of a net difference in polymer processing, influencing the thin-film morphology, and to the absence of π-stacking interactions in films processed with **P1.1**. These important results further reinforce the necessity to attain number-average molecular weights that are sufficiently high to be able to remove the largest extent of this dependence from the polymer performance data.

Upon comparing **P2.1** (M_n = 18.3 kDa in TCB) to **P2.2** (M_n = 36.1 kDa in TCB), the transistor mobility gains about 2 orders of magnitude, raising from 3×10^{-4} to 4×10^{-2} cm^2 V^{-1} s^{-1}, in a drop-cast transistor subsequently annealed at a temperature identified as providing the best device performance for the respective drop-cast polymers (Figure S16). This result is consistent with the pronounced increase in lamellar orientation and the decrease in *d*-spacing observed in the bulk of the polymer by 2D-WAXS for the larger molecular weight fraction (see Figure 1c and d), as well as with the slight increase in π-stacking intensity seen on thermal annealing in general (see Figure S1c and d).

Similarly, the device thermal annealing conditions were found to affect the performance of **P3** and **P4** in FETs (though to a lesser extent), with hole mobilities increasing to values as high as 5×10^{-2} cm^2 V^{-1} s^{-1} in the case of **P4** after annealing, and a peak mobility of 1×10^{-2} cm^2 V^{-1} s^{-1} for **P3** after annealing. Figure 7 illustrates the trend in field-effect hole mobilities observed following the successive thermal annealing steps subjected to the drop-cast transistor devices made with **P2.2**, **P3**, and **P4**. In the case of **P4**, the high as-cast mobility value of 2×10^{-2} cm^2 V^{-1} s^{-1} is worth emphasizing considering

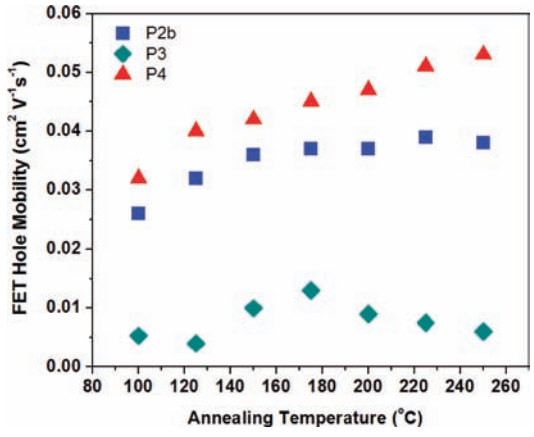

Figure 7. Evolution of field-effect hole mobilities at saturation (μ_{sat}, cm^2 V^{-1} s^{-1}) for **P2.2**, **P3**, and **P4** drop-cast on HMDS-passivated SiO_2 as a function of annealing temperature (annealing maintained 15 min each time).

commercial viability aspects, and is in excellent agreement with the ability of this polymer to "crystallize" from the processing solvent (see Figure S1f and previously reported work[14c]), without being subjected to more elevated temperatures as necessary with its counterpart **P2.2**.

Interestingly, in comparing the linear octyl-substituted **P1.2**, whose highest achievable molecular weight was found to not exceed 12.7 kDa, to its branched 2-ethylhexyl-substituted counterpart **P5.1**, a clear FET performance enhancement was observed, thus reaching mobility values as high as 0.1 cm^2 V^{-1} s^{-1} in drop-cast devices (see Table 2). Figure S17 shows the FET transfer curve and the corresponding output characteristics at various applied gate-voltages for **P5.1**. Similarly here, the device properties of **P5.1** are consistent with the high degree of microstructural order observed by 2D-WAXS (see Figure 2). Following those considerations, it is further worth noting that the molecular weight of **P5.1** remains relatively modest when compared to that attained with **P2.2**, and the synthesis of a longer backbone distribution is expected to lead to even higher mobilities as no clear evidence that a limit in terms of FET performance as been reached so far in our work with **P5**.

For comparison of different processing methods, **P1**–**P5** were integrated in spin-cast (as opposed to the above-discussed drop-cast) thin-film transistors (HMDS-passivated SiO_2); the devices were all subjected to a thermal annealing step at 200 °C (15 min), since all semiconducting copolymers had previously shown close to peak performance after exposure at 200 °C in this device configuration. Field-effect mobilities and current on/off ratios are reported in Table 2. In the present device configuration, the charge-carrier mobilities for the polymers are less than 2 orders of magnitude lower than those determined with the drop-cast architecture, which also points toward a certain degree of structural order for the spin-coated polymers. Here, **P2.2** and **P5.1** show the highest hole mobilities -7×10^{-3} and 5×10^{-3} cm^2 V^{-1} s^{-1}, respectively, and the mobility values obtained for **P3** and **P4** are relatively close to these, in agreement with the processing method employed.

Thin-Film X-ray Diffraction Analysis. X-ray diffraction (XRD) was performed on polymer thin films (for **P1.2**, **P2.2**, **P3**, **P4**, and **P5.1**) obtained following the same solution-processing and temperature-annealing conditions as those employed during the transistor fabrication. As reported in Table 2, the *d*-spacings estimated by XRD closely followed the trend set by the 2D wide-angle X-ray scattering method, with values only slightly higher than those estimated from the polymer fibers; this reinforces the relevance of the measurements performed from the bulk semiconducting materials (vide supra). For example, **P2.2**, **P4**, and **P5.1** also show the smallest interlamellar distances in drop-cast films, estimated to be as low as 1.79, 1.83, and 1.74 nm, respectively. The diffractograms for the drop-cast polymer films are shown in Figure S18. Interestingly, the Bragg reflection seen at the small angles for each polymer is relatively pronounced and nearly identical in intensity across the analogous series. In this sense, looking at mechanically oriented fibers by 2D-WAXS provided much deeper insight into the varying degrees of microstructural order attained by each polymer upon thermal annealing. Other XRD experiments (low-temperature annealing) revealed that only **P4** shows the ability to 'crystallize' from the processing solvent without being subjected to more elevated temperatures as necessary with its counterparts **P2.2** and **P5.1**.

dx.doi.org/10.1021/ja301898h | *J. Am. Chem. Soc.* 2012, 134, 8944–8957

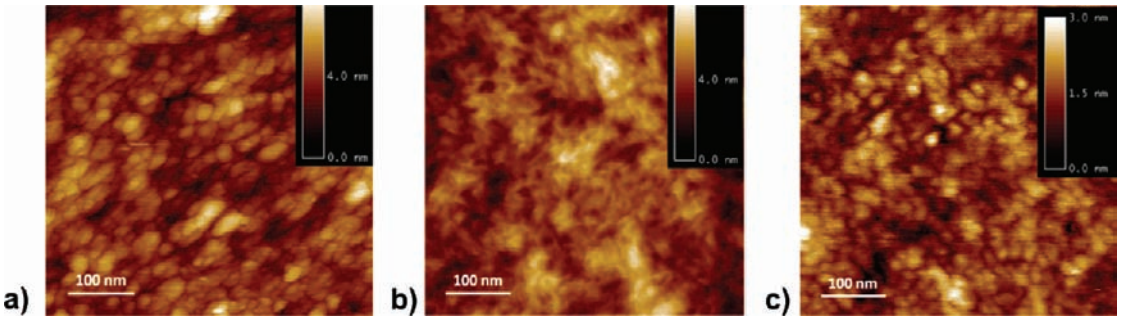

Figure 8. AFM tapping-mode images (heights) of (a) **P1.2** and (b) **P2.2**, drop-cast on HMDS-treated SiO_2 (the film surfaces are represented), along with that of (c) **P3** spin-cast on HMDS-treated SiO_2 for comparison. Each device received a postpolymer processing thermal treatment of 15 min at a temperature identified as providing the best device performance (vide supra).

Table 3. Solar Cell Device Performance Observed for P1.2, P2.2, P3, P4, P5.1, and P5.2 at Optimized Polymer:$PC_{71}BM$ blend Composition (w/w) (AM1.5G illumination, 100 mW cm^{-2})[a]

	solar cell devices						hole-only devices	
polymer	PX:$PC_{71}BM$	thick.	J_{SC}	V_{OC}	FF	PCE	μ(PX)	μ(PX:$PC_{71}BM$)
P1.2	1:2	110	8.52	0.63	37	2.01	1.0×10^{-5}	1.0×10^{-5}
P2.2	1:2	120	9.80	0.51	49	2.44	3.0×10^{-4}	1.9×10^{-4}
P3	1:2	105	6.65	0.70	34	1.58	2.0×10^{-5}	1.0×10^{-5}
P4	1:2	105	7.89	0.59	43	2.02	1.0×10^{-3}	4.8×10^{-4}
P5.1	1:1.5	110	12.29	0.61	51	3.80	8.0×10^{-5}	2.2×10^{-4}
P5.2	1:1.5	110	**13.44**	**0.62**	**55**	**4.59**	2.4×10^{-4}	6.8×10^{-4}

[a]Thickness of the active layer (nm), short-circuit current density (mA cm^{-2}), open-circuit voltage (V), device fill-factor (%), power conversion efficiency (%). The devices were subjected to a post-polymer processing thermal treatment at 200 °C (for 1−5 min), under inert atmosphere. The solar cell device structure is ITO/PEDOT/PX:$PC_{70}BM$/LiF/Al. All the solar cell results were collected under atmospheric conditions. Zero-field hole mobility (cm^2 V^{-1} s^{-1}) in the pristine copolymers **P1.2**, **P2.2**, **P3**, **P4**, **P5.1**, and **P5.2**, and in the polymer phase of the optimized blends (PX:$PC_{71}BM$). Values derived from hole-only devices (ITO/PEDOT-PSS/PX or PX:PCBM/Au), and obtained by fitting the *J*−*V* data to trap-free single-carrier SCLC model. Devices with post-polymer processing thermal treatment at 150 °C (5-6 min).

AFM Topography. In addition to the X-ray analyses performed for the bulk and thin-film semiconducting polymers, atomic force microscopy (AFM) was employed in the tapping mode to image the topography of the transistor device thin-film active layers obtained from the two distinct deposition methods applied in this study (drop-cast versus spin-cast deposition). The analysis was carried out to probe the film-forming propensities across the polymer series, and to tentatively correlate microstructural order-directed morphology with device performance. While the morphology may arguably differ at the polymer−dielectric interface, it is expected that a certain degree of macroscopic and microstructural order is retained, for the drop-cast films in particular.

Figure 8 illustrates the various morphologies obtained for the drop-cast (Figure 8a,b and Figure S19) and spin-cast (Figure 8c and Figure S20) depositions of the semiconducting polymers on HMDS-passivated SiO_2. While the topographic patterns for **P1.2** and **P3** appear to possess a similar nodular character when compared to others, the p-type mobility of **P1.2** (1×10^{-2} cm^2 V^{-1} s^{-1}) and that of **P3** (1×10^{-2} cm^2 V^{-1} s^{-1}) at peak performance are also about half an order of magnitude less than those of their counterparts **P2.2** (4×10^{-2} cm^2 V^{-1} s^{-1}) and **P4** (5×10^{-2} cm^2 V^{-1} s^{-1}) in drop-cast devices. The improved charge-carrier mobilities of **P2.2** and **P4** may stem from their much more fibrilar morphology in thin films, suggesting the presence of domains with more pronounced alignment in comparison with the nodular case. Following the same argument, the presence of more extended ordered domains is suggested in the films of **P5.1** (Figure S19e). The more "crystalline" character of **P5.1** has previously been evidenced by 2D-WAXS (see Figure 2). In parallel, **P5.1** shows an increase in hole mobility (1×10^{-1} cm^2 V^{-1} s^{-1}) of about half an order of magnitude in comparison with that of **P2.2** and **P4**. In comparison, the morphologies obtained from spin-casting the semiconducting polymers onto HMDS-passivated SiO_2 were found to be significantly more homogeneous as exemplified with **P3** in Figure 8c and further detailed in Figure S20. Beyond the apparent film similarities, it is worth noting that the image relative to **P5.1** does show coarser features reminiscent of those observed in the drop-cast films (Figure S19e), a feature induced by the more pronounced propensity of the polymer to self-assemble into structured domains (as suggested by the 2D-WAXS analysis).

Solar Cell Device Fabrication and Testing. The photovoltaic properties of **P1**−**P5** were examined in donor−acceptor bulk heterojunction solar cells (BHJs) employing (6,6)-phenyl-C_{71}-butyric acid methyl ester ($PC_{71}BM$) as the electron acceptor. All solar cell results were collected under atmospheric conditions and simulated AM 1.5G solar illumination (at an irradiation intensity of 100 mW cm^{-2}). The copolymer-$PC_{71}BM$ blends were spin-cast from chlorobenzene in devices using PEDOT-PSS-coated ITO glass substrates. The blend compositions, as well as the thickness of the active layer to be solution-processed, were optimized. The results are summarized in Table 3. The semiconducting active layers were subjected to appropriate thermal annealing before top electrode deposition (see Table 3). Figure 9 superimposes the *J*−*V* curves for devices made with **P1.2**, **P2.2**, **P3**, **P4**, and **P5.2** at optimized thickness and polymer:$PC_{71}BM$ composition.

dx.doi.org/10.1021/ja301898h | *J. Am. Chem. Soc.* 2012, 134, 8944−8957

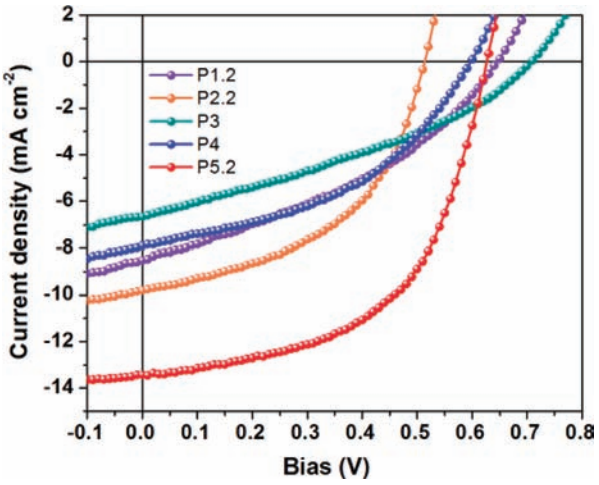

Figure 9. *I*–*V* curves of **P1.2**, **P2.2**, **P3**, **P4**, and **P5.2** based PSCs (at best polymer:PCBM composition) under AM 1.5 solar illumination, 100 mW cm^{-2}. Devices with postpolymer processing thermal treatment at 70 °C (30 min). The device structure is ITO/PEDOT/PX:PC$_{70}$BM/LiF/Al with PX = **P1.2**, **P2.2**, **P3**, **P4**, or **P5.2**.

As shown in Table 3, a polymer:PC$_{71}$BM ratio of 1:2 (by weight) was found to be optimum across the entire linearly substituted polymer series **P1**–**P4**. Here, the results obtained throughout the structural X-ray analyses of the polymers, and the charge-transport study in transistors, justified using the largest molecular weight fractions of **P1** and **P2**, respectively **P1.2** and **P2.2**, for the solar cell device fabrication. The polymer that provided the most limited PV device performance was **P3**, which showed a relatively modest power conversion efficiency (PCE) of 1.58%, correlated to the low intensity of photogenerated current (ca. 7 mA cm^{-2}). Interestingly, **P3** shows the least pronounced degree of achievable microstructural organization (as evidenced by 2D-WAXS), with no observable π-stacking, relatively long interlamellar distances (d = 1.94 nm), and a clear lack of lamellar orientation (see Figure S1e). In comparison, **P1.2** and **P4** show almost exactly the same device performance, with PCE values in the order of 2% and fill factors (FF) exceeding 35%. In the linearly substituted polymer series **P1**-**P4**, **P2.2** represents the most effective system in BHJs with PC$_{71}$BM, demonstrating the highest photogenerated current densities (ca. 10 mA cm^{-2}), a substantial FF of 49%, and up to 2.44% of PCE. Here again, when looking at the results obtained by 2D-WAXS (see Figure 1d), **P2.2** shows the more pronounced degree of achievable structural organization, with a narrow d-spacings of 1.75 nm and higher-order small-angle reflections suggesting better packing properties.

However, it is only by varying the side-chain substitution pattern of **P1** to yield the polymer analogue **P5**, here represented by its molecular weight fraction **P5.2** (M_n = 26.4 kDa in TCB), that an outstanding performance enhancement is observed. In this case, the measured photogenerated current density exceeds 13 mA cm^{-2}, and the FF improves by some 50% when compared to that of the linearly substituted analogue **P1.2** (FF going from 37% to 55%). Overall, the measured PCE was found to average 4.59%, in good agreement with other recent contributions emphasizing the photovoltaic properties of this particular system.[3d,14a,b,15] The EQE data of the corresponding **P5.2**-based BHJ device is shown as Figure S21, in which the long wavelength maximum peaking at 51% of EQE is assigned to the long wavelength absorption band of the polymer. The short wavelength maximum can be attributed to the absorption by PC$_{71}$BM combined with that of the short wavelength absorption band of the polymer (see Table 3), and the onset of photocurrent at about 900 nm is in agreement with the polymer thin-film optical absorption (also shown in Figure S21). Considering that no small molecule processing additive was used during device preparation (in order to avoid interfering with the self-assembling properties of the materials described in this study), the excellent results obtained with **P5.2** versus **P1.2** could be the consequence of (i) the higher molecular weight, (ii) its greater ability to order (as suggested by 2D-WAXS), or more likely (iii) a combination of these two factors. As suggested earlier in this report, it is expected that the presence of the 2-ethyl substituent appended to the hexyl main chain of the solubilizing side groups promotes favorable self-assembly of the polymer backbone by imparting proper interchain spacing, less hindered torsional motions between repeat units, and adequate processing ability. In any case, differences in carrier mobility should be expected to result from these intrinsic structural disparities (vide infra).

Inspecting Figure 9 further, it is essential to note that the open-circuit voltages (V_{OC}) observed for the devices made are system-dependent and vary considerably across the polymer series: being as low as 0.51 eV for **P1.2** and as high as 0.70 eV for **P3**. Given the close oxidation potentials estimated electrochemically for the polymers and the comparable IPs calculated by DFT, it appears that the variations in V_{OC} observed across the polymer series could depend less on the intrinsic energetics of the individual polymer chains, than on the degree of microstructural order in the polymer-rich domains and the film morphology for example.[32]

Insight into the morphology obtained on blending **P5.2** with the electron-acceptor PC$_{71}$BM at optimized polymer:fullerene composition is provided in Figure S22. AFM was used in the tapping-mode to image device regions where the top contacts were not present. The 2D image of the **P5** based device surface shown in Figure S22 reveals a relatively nodular morphology (sharp features of 10 nm in height, rms roughness = 1.567 nm) where large domains of higher heights are dispersed within the active layer. Consistent with other contributions on the topic,[33] the larger domains with taller heights are tentatively assigned to the PCBM-rich phase, with no indication of "overgrown" PC$_{71}$BM-cluster formation. In fact, it is now well established that a certain extent of phase separation between donor and acceptor in the BHJ remains a necessary condition in the formation of the bicontinuous interpenetrating network configuration desired to obtain efficient solar cell devices.[34] In contrast, and as previously proposed,[34,35] a pronounced phase segregation (demixing) between PC$_{71}$BM and the polymer (not observed here) would likely impede the BHJ device performance by confining the dissociated charges to the segregated domains.

Space Charge-Limited Current–Voltage Measurements. Considering the distinct solar cell responses observed across the polymer series **P1**–**P5** in BHJs with PC$_{71}$BM, inspection of the space charge limited current (SCLC) in the composite active layers (at optimized composition) was envisaged to correlate carrier transport and device performance. With the photogenerated current in donor–acceptor excitonic solar cells dominated by a combination of exciton generation and dissociation rates, and by the recombination processes, the charge transport in the p-type and n-type semiconductors

should be balanced to avoid the buildup of charges commonly observed in materials with low intrinsic drift carrier mobilities and short carrier lifetimes.[36] In this regard, the SCL transport in the pristine polymers was examined to gain insight into the influence of microstructural order on the charge-carrier properties of **P1**−**P5** in vertically stacked devices (i.e., factoring out the field effect dependence as in thin-film transistors). The electron mobility in the PCBM-rich phase of a polymer:PCBM blend has previously been determined to be on the order of 10^{-3} cm^2 V^{-1} s^{-1}.[37]

In systems where the dark current is space-charge limited (i.e., in media with low mobility and low intrinsic carrier concentration), the mobility can be simply extracted from the current−density−voltage response, as illustrated by the Mott-Gurney equation for trap-free SCL currents:

$$J = 9/8\mu\varepsilon\frac{V^2}{d^3} \quad (2)$$

where ε is the dielectric constant, μ is the charge-carrier mobility, and d is the sample thickness. Hole-only devices with gold electron-blocking counter electrodes were fabricated with the following configuration: ITO/PEDOT-PSS/polymer or polymer:$PC_{71}BM$/Au. The films were annealed at 150 °C for 5−6 min prior to Au deposition.

Figure S23 shows the empirical dark current densities passing across hole-only devices made with the pristine copolymers **P1.2**, **P2.2**, **P3**, **P4**, and **P5.1**. The applied voltage V was corrected for the built-in voltage V_{bi} resulting from the difference in work function between electrodes, and appears as the effective electric field E_{eff} to facilitate comparison of devices with different thicknesses. Here, it should be noted that, in all cases, the current densities were found to scale quadratically with the applied voltage (see Figure S23, inset), hence reflecting space-charge-limited transport.

From the results presented in Table 3, it should be noted that the pristine copolymers **P2.2** and **P4** demonstrate hole mobilities higher than those of **P1.2** and **P3** by more than 1 order of magnitude, following the SCL transport model governed by eq 1. Further, it is interesting to note that these results can be correlated to the trend set by the 2D-WAXS polymer fiber analysis (vide supra), whereby **P2.2** and **P4** showed particularly small π-stacking distances (3.6 Å) and the shortest lamellar distances (1.75 and 1.84 nm, respectively), while essentially no π-stacking and a large d-spacing were observed in the case of **P3** for instance. With the relatively low molecular weight of **P1.2** (in comparison with **P2.2** and **P4**) and its higher concentration of chain-ends possibly hindering the formation of well-ordered nanoscale domains, more modest charge-carrier mobilities had been anticipated for this polymer. In parallel, the especially high zero-field mobility value estimated with **P4** (1.0×10^{-3} cm^2 V^{-1} s^{-1}) is nearly identical to that observed in spin-cast bottom-gate/bottom-contact FET devices (7×10^{-4} cm^2 V^{-1} s^{-1}), hence possibly suggesting a certain isotropy in the hole transport properties of the polymer (although direct correlations are not systematic in considering SCL versus FET charge-carrier measurements[38]). This result correlates with the introduction of unsubstituted conjugated spacers along the backbone of **P4** that further diminish the concentration of solubilizing side-chains along the π-conjugated main-chain.[14c] Overall, and as illustrated in Figure S23, the device current densities at low device biases (actual device bias range in solar cells) increase on going from the pristine polymer **P1.2**, to **P3**, to **P4**, and to **P2.2**, likely as a result of (i) increasingly prominent ordering abilities and (ii) increasingly higher polymer molecular weights.

It is worth noting that neither **P5.1** nor **P5.2** reveal drastically superior hole mobilities by the SCLC approach, such that the clear photovoltaic performance enhancement observed in Figure 9 could result from a simple morphology effect (in absence of further insight into the polymer charge-transport characteristics in blends with $PC_{71}BM$). In fact, the zero-field hole mobilities in blends of **P5** with $PC_{71}BM$ (as optimized to best photoresponse) are found to be more than one (**P5.1**) and nearly two (**P5.2**) orders of magnitude larger than that for **P1.2** (see Table 3), hence strongly supporting the considerably improved photovoltaic response seen in the branched alkyl-substituted analogue **P5.2** based devices. Importantly, the hole transport in the polymer−fullerene blends is almost systematically lower than that in the pristine polymers, except in the case of **P5.2**, thus pointing to a favorable intimate polymer−fullerene self-assembly achieved on blending the donor and the acceptor in the latter case. Favorable changes in polymer−fullerene self-assembly have previously been proposed on mixing PPV-based donor polymers and PCBM in order to account for hole mobility enhancements in BHJs.[36b,39] This phenomenon has been attributed to an increase in polymer-backbone ordering in the presence of PCBM.

■ CONCLUSIONS

Following "donor−acceptor" principles, we have designed and synthesized a series of low-band-gap π-conjugated polymer analogues that combine the electron-rich dithienosilole (DTS) moiety, unsubstituted thiophene spacers, and the electron-deficient core 2,1,3-benzothiadiazole (BTD). These polymers (**P1**−**P5**) were designed to incorporate (i) distinct ratios of electron-rich to electron-deficient moieties in the monomer repeat unit, and (ii) variations (i.e., concentration and bulkiness) of the solubilizing side-chains along the backbones, with the goal of identifying synthetic principles that impart clear improvements in carrier mobilities in low-band-gap polymers. In this contribution, important correlations were drawn between the structural variations imparted to the polymer backbones and their charge-transport properties in thin films, using OTFT and OPV devices as platforms for the study. Based on a combination of X-ray techniques (2D-WAXS and XRD) supported by SS-NMR and AFM, we emphasize the key role of (i) molecular weight distribution and (ii) the nature of the solubilizing substituents appended to the backbones on the degree of microstructural organization that can be attained with each polymer. Overall, small structural changes induced along the DTS-BTD backbones resulted in notable variations in charge transport and photovoltaic properties in thin-film devices. Of all the DTS-BTD backbones inspected, the highest molecular weight fraction (**P5.2**) of the strictly alternating donor−acceptor derivative **P5** functionalized with 2-ethylhexyl branched substituents stands out by demonstrating field-effect mobilities as high as 0.1 cm^2 V^{-1} s^{-1} in bottom-gate/bottom-contact transistors. The same material approaches a space-charge-limited (SCL) hole mobility of 10^{-3} cm^2 V^{-1} s^{-1} in hole-only devices composed of a BHJ of the polymer with the electron-acceptor $PC_{71}BM$; the control solar cells show PCEs on the order of 4.6% in the absence of small molecule additive-assisted device processing (i.e., no morphology control), confirming the importance of charge transport in DTS-BTD−

dx.doi.org/10.1021/ja301898h | J. Am. Chem. Soc. 2012, 134, 8944−8957

based OPV devices. These results clearly reinforce the argument that maximizing charge transport in conjugated polymers implies that the appropriate combination of (i) repeat unit structure, (ii) molecular weight distribution, and (iii) solubilizing side-chain substituents be found for a given set of aromatic building units, as each of these parameters impacts polymer self-assembling properties. Remarkably, we found a large dependence of the ionization potentials of the polymers estimated by electrochemical methods on polymer packing. These empirical results may have important consequences on future material study and device applications.

■ ASSOCIATED CONTENT

Supporting Information

Experimental details, synthesis of the monomers and polymers, additional 2D-WAXS, SS-NMR, CV and DPV data, OTFT and OPV device fabrication details, XRD, AFM, EQE, SCLC data, DFT calculations. This material is available free of charge via the Internet at http://pubs.acs.org.

■ AUTHOR INFORMATION

Corresponding Author

reynolds@chemistry.gatech.edu

Notes

The authors declare no competing financial interest.

■ ACKNOWLEDGMENTS

We acknowledge the funding of this work as follows. J.R.R.: the Air Office of Scientific Research (FA9550-09-1-0320) for new materials development. J.R.R. and F.S.: the Office of Naval Research (N00014-11-1-0245) for transport measurements and device construction/testing. J.-L.B.: the Office of Naval Research (N00014-11-1-0211) for computational studies. K.M.: the German Science Foundation (Korean-German IR TG), the European Community's Seventh Framework Programme ONE-P (grant agreement no. 212311), DFG Priority Program SPP 1355, DFG MU 334/32-1, DFG Priority Program SPP 1459, and ESF Project GOSPEL (ref no.: 09-EuroGRAPHENE-FP-001) for characterization studies. M.R.H. acknowledges Dr. Robert Graf for helpful discussions and Prof. Hans Wolfgang Spiess for his continued support. P.M.B. acknowledges Dr. Uwe Rietzler and Dr. Rüdiger Berger for their support at the AFM facilities of MPIP-Mainz.

■ REFERENCES

(1) (a) Murphy, A. R.; Fréchet, J. M. J. *Chem. Rev.* **2007**, *107*, 1066–1096. (b) Allard, S.; Forster, M.; Souharce, B.; Thiem, H.; Scherf, U. *Angew. Chem., Int. Ed.* **2008**, *47*, 4070–4098. (c) Arias, A. C.; MacKenzie, J. D.; McCulloch, I.; Rivnay, J.; Salleo, A. *Chem. Rev.* **2010**, *110*, 3–24. (d) Tsao, H. N.; Müllen, K. *Chem. Soc. Rev.* **2010**, *39*, 2372–2386. (e) Anthony, J. E.; Facchetti, A.; Heeney, M.; Marder, S. R.; Zhan, X. *Adv. Mater.* **2010**, *22*, 3876–3892. (f) Facchetti, A. *Chem. Mater.* **2010**, *23*, 733–758. (g) Usta, H.; Facchetti, A.; Marks, T. J. *Acc. Chem. Res.* **2011**, *44*, 501–510.

(2) Thomas, S. W.; Joly, G. D.; Swager, T. M. *Chem. Rev.* **2007**, *107*, 1339–1386.

(3) (a) Bundgaard, E.; Krebs, F. C. *Sol. Energy Mater. Sol. Cells* **2007**, *91*, 954–985. (b) Thompson, B. C.; Fréchet, J. M. J. *Angew. Chem., Int. Ed.* **2008**, *47*, 58–77. (c) Roncali, J. *Acc. Chem. Res.* **2009**, *42*, 1719–1730. (d) Dennler, G.; Scharber, M. C.; Brabec, C. J. *Adv. Mater.* **2009**, *21*, 1323–1338. (e) Chen, J.; Cao, Y. *Acc. Chem. Res.* **2009**, *42*, 1709–1718. (f) Brunetti, F. G.; Kumar, R.; Wudl, F. *J. Mater. Chem.* **2010**, *20*, 2934–2948. (g) Boudreault, P.-L. T.; Najari, A.; Leclerc, M. *Chem. Mater.* **2011**, *23*, 456–469. (h) Walker, B.; Kim, C.; Nguyen, T.-Q. *Chem. Mater.* **2011**, *23*, 470–482.

(4) (a) Beaujuge, P. M.; Reynolds, J. R. *Chem. Rev.* **2010**, *110*, 268–320. (b) Beaujuge, P. M.; Amb, C. M.; Reynolds, J. R. *Acc. Chem. Res.* **2010**, *43*, 1396–1407. (c) Amb, C. M.; Dyer, A. L.; Reynolds, J. R. *Chem. Mater.* **2010**, *23*, 397–415.

(5) Li, J.; Dierschke, F.; Wu, J.; Grimsdale, A. C.; Müllen, K. *J. Mater. Chem.* **2006**, *16*, 96–100.

(6) McCulloch, I.; Heeney, M.; Bailey, C.; Genevicius, K.; MacDonald, I.; Shkunov, M.; Sparrowe, D.; Tierney, S.; Wagner, R.; Zhang, W.; Chabinyc, M. L.; Kline, R. J.; McGehee, M. D.; Toney, M. F. *Nat. Mater.* **2006**, *5*, 328–333.

(7) (a) McCulloch, I.; Heeney, M.; Chabinyc, M. L.; DeLongchamp, D.; Kline, R. J.; Cölle, M.; Duffy, W.; Fischer, D.; Gundlach, D.; Hamadani, B.; Hamilton, R.; Richter, L.; Salleo, A.; Shkunov, M.; Sparrowe, D.; Tierney, S.; Zhang, W. *Adv. Mater.* **2009**, *21*, 1091–1109. (b) Zhang, X.; Hudson, S. D.; DeLongchamp, D. M.; Gundlach, D. J.; Heeney, M.; McCulloch, I. *Adv. Funct. Mater.* **2010**, *20*, 4098–4106. (c) Wang, C.; Jimison, L. H.; Goris, L.; McCulloch, I.; Heeney, M.; Ziegler, A.; Salleo, A. *Adv. Mater.* **2010**, *22*, 697–701.

(8) Jack, E. P.; Alex, C. M.; Brian, E. H.; Shawn, R. S.; Michael, D. M.; Martin, H.; Iain, M. *Appl. Phys. Lett.* **2008**, *92*, 113309.

(9) Cates, N. C.; Gysel, R.; Beiley, Z.; Miller, C. E.; Toney, M. F.; Heeney, M.; McCulloch, I.; McGehee, M. D. *Nano Lett.* **2009**, *9*, 4153–4157.

(10) (a) Havinga, E. E.; Hoeve, W.; Wynberg, H. *Polym. Bull.* **1992**, *29*, 119–126. (b) Havinga, E. E.; Hoeve, W.; Wynberg, H. *Synth. Met.* **1993**, *55*, 299–306.

(11) Bijleveld, J. C.; Zoombelt, A. P.; Mathijssen, S. G. J.; Wienk, M. M.; Turbiez, M.; de Leeuw, D. M.; Janssen, R. A. J. *J. Am. Chem. Soc.* **2009**, *131*, 16616–16617.

(12) (a) Wienk, M. M.; Turbiez, M.; Janssen, R. A. J. *Adv. Mater.* **2008**, *20*, 2556–2560. (b) Zou, Y.; Gendron, D.; Badrou-Aich, R.; Najari, A.; Tao, Y.; Leclerc, M. *Macromolecules* **2009**, *42*, 2891–2894. (c) Sonar, P.; Singh, S. P.; Li, Y.; Soh, M. S.; Dodabalapur, A. *Adv. Mater.* **2010**, *22*, 5409–5413. (d) Bijleveld, J. C.; Gevaerts, V. S.; Di Nuzzo, D.; Turbiez, M.; Mathijssen, S. G. J.; de Leeuw, D. M.; Wienk, M. M.; Janssen, R. A. J. *Adv. Mater.* **2010**, *22*, E242–E246. (e) Li, Y.; Singh, S. P.; Sonar, P. *Adv. Mater.* **2010**, *22*, 4862–4866. (f) Bronstein, H.; Chen, Z.; Ashraf, R. S.; Zhang, W.; Du, J.; Durrant, J. R.; Shakya Tuladhar, P.; Song, K.; Watkins, S. E.; Geerts, Y.; Wienk, M. M.; Janssen, R. A. J.; Anthopoulos, T.; Sirringhaus, H.; Heeney, M.; McCulloch, I. *J. Am. Chem. Soc.* **2011**, *133*, 3272–3275.

(13) (a) Usta, H.; Lu, G.; Facchetti, A.; Marks, T. J. *J. Am. Chem. Soc.* **2006**, *128*, 9034–9035. (b) Lu, G.; Usta, H.; Risko, C.; Wang, L.; Facchetti, A.; Ratner, M. A.; Marks, T. J. *J. Am. Chem. Soc.* **2008**, *130*, 7670–7685.

(14) (a) Hsiang-Yu, C.; Jianhui, H.; Amy, E. H.; Hoichang, Y.; Houk, K. N.; Yang, Y. *Adv. Mater.* **2010**, *22*, 371–375. (b) Scharber, M. C.; Koppe, M.; Gao, J.; Cordella, F.; Loi, M. A.; Denk, P.; Morana, M.; Egelhaaf, H.-J.; Forberich, K.; Dennler, G.; Gaudiana, R.; Waller, D.; Zhu, Z.; Shi, X.; Brabec, C. J. *Adv. Mater.* **2010**, *22*, 367–370. (c) Beaujuge, P. M.; Pisula, W.; Tsao, H. N.; Ellinger, S.; Mullen, K.; Reynolds, J. R. *J. Am. Chem. Soc.* **2009**, *131*, 7514–7515. (d) Piliego, C.; Holcombe, T. W.; Douglas, J. D.; Woo, C. H.; Beaujuge, P. M.; Fréchet, J. M. J. *J. Am. Chem. Soc.* **2010**, *132*, 7595–7597. (e) Chen, H.-Y.; Hou, J.; Zhang, S.; Liang, Y.; Yang, G.; Yang, Y.; Yu, L.; Wu, Y.; Li, G. *Nat. Photonics* **2009**, *3*, 649–653.

(15) Hou, J.; Chen, H.-Y.; Zhang, S.; Li, G.; Yang, Y. *J. Am. Chem. Soc.* **2008**, *130*, 16144–16145.

(16) Waldauf, C.; Morana, M.; Denk, P.; Schilinsky, P.; Coakley, K.; Choulis, S. A.; Brabec, C. J. *Appl. Phys. Lett.* **2006**, *89*, 233517–233513.

(17) (a) Pisula, W.; Tomovic, Z.; Simpson, C.; Kastler, M.; Pakula, T.; Mullen, K. *Chem. Mater.* **2005**, *17*, 4296–4303. (b) Zhang, M.; Tsao, H. N.; Pisula, W.; Yang, C.; Mishra, A. K.; Mullen, K. *J. Am. Chem. Soc.* **2007**, *129*, 3472–3473. (c) Tsao, H. N.; Cho, D.; Andreasen, J. W.; Rouhanipour, A.; Breiby, D. W.; Pisula, W.; Müllen, K. *Adv. Mater.* **2008**, *21*, 209–212.

(18) Note: Difference in heights of the triangles formed by the vectors that originate at the Si atom and extend to the terminal C on the alkyl chain for a DTS molecule with the alkyl chains. The functional used includes dispersion corrections, an important parameter to take into account in the description of alkyl−alkyl chain interactions.
(19) Schmidt-Rohr, K.; Spiess, H. W. *Multidimensional Solid-State NMR and Polymers*, 1994.
(20) (a) Schleyer, P. V.; Maerker, C.; Dransfeld, A.; Jiao, H.; Hommes, N. J. R. V. *J. Am. Chem. Soc.* **1996**, *118*, 6317−6318. (b) Lazzeretti, P. *Prog. Nucl. Magn. Reson. Spectrosc.* **2000**, *36*, 1−88. (c) Brown, S. P.; Spiess, H. W. *Chem. Rev.* **2001**, *101*, 4125−4155. (d) Brown, S. P. *Prog. Nucl. Magn. Reson. Spectrosc.* **2007**, *50*, 199−251.
(21) (a) Farnan, I.; Grandinetti, P. J.; Baltisberger, J. H.; Stebbins, J. F.; Werner, U.; Eastman, M. A.; Pines, A. *Nature* **1992**, *358*, 31−35. (b) Youngman, R. E.; Haubrich, S. T.; Zwanziger, J. W.; Janicke, M. T.; Chmelka, B. F. *Science* **1995**, *269*, 1416−1420. (c) Cadars, S.; Lesage, A.; Pickard, C. J.; Sautet, P.; Emsley, L. *J. Phys. Chem. A* **2009**, *113*, 902−911. (d) Hedin, N.; Graf, R.; Christiansen, S. C.; Gervais, C.; Hayward, R. C.; Eckert, J.; Chmelka, B. F. *J. Am. Chem. Soc.* **2004**, *126*, 9425−9432.
(22) (a) Pines, A.; Gibby, M. G.; Waugh, J. S. *J. Chem. Phys.* **1973**, *59*, 569−590. (b) Feike, M.; Demco, D. E.; Graf, R.; Gottwald, J.; Hafner, S.; Spiess, H. W. *J. Magn. Reson., Ser. A* **1996**, *122*, 214−221. (c) Feike, M.; Graf, R.; Schnell, I.; Jager, C.; Spiess, H. W. *J. Am. Chem. Soc.* **1996**, *118*, 9631−9634. (d) Laage, S.; Marchetti, A.; Sein, J.; Pierattelli, R.; Sass, H. J.; Grzesiek, S.; Lesage, A.; Pintacuda, G.; Emsley, L. *J. Am. Chem. Soc.* **2008**, *130*, 17216.
(23) Tsao, H. N.; Cho, D. M.; Park, I.; Hansen, M. R.; Mavrinskiy, A.; Yoon, D. Y.; Graf, R.; Pisula, W.; Spiess, H. W.; Müllen, K. *J. Am. Chem. Soc.* **2011**, *133*, 2605−2612.
(24) Hansen, W. N.; Hansen, G. J. *Phys. Rev. A* **1987**, *36*, 1396−1402.
(25) Pavlishchuk, V. V.; Addison, A. W. *Inorg. Chem. Acta* **2000**, *298*, 97−102.
(26) Bard, A. J.; Faulkner, L. R. *Electrochemical Methods*, 2nd ed.; John Wiley & Sons: Hoboken, NJ, 2001.
(27) Rasmussen, S. C.; Ogawa, K.; Rothstein, S. D. In *The Handbook of Organic Electronics and Photonics*; Nalwa, H. S., Ed.; American Scientific Publishers: Stevenson Ranch, CA, 2008; Vol. *1*.
(28) Oldham, K. B.; Myland, J. C. *Fundamentals of Electrochemical Science*; Academic Press, Inc.: San Diego, CA, 1994.
(29) (a) Müller, C.; Wang, E.; Andersson, L. M.; Tvingstedt, K.; Zhou, Y.; Andersson, M. R.; Inganäs, O. *Adv. Funct. Mater.* **2010**, *20*, 2124−2131. (b) Tong, M.; Cho, S.; Rogers, J. T.; Schmidt, K.; Hsu, B. B. Y.; Moses, D.; Coffin, R. C.; Kramer, E. J.; Bazan, G. C.; Heeger, A. J. *Adv. Funct. Mater.* **2010**, *20*, 3959−3965. (c) Gadisa, A.; Oosterbaan, W. D.; Vandewal, K.; Bolsée, J.-C.; Bertho, S.; D'Haen, J.; Lutsen, L.; Vanderzande, D.; Manca, J. V. *Adv. Funct. Mater.* **2009**, *19*, 3300−3306. (d) Oosterbaan, W. D.; Vrindts, V.; Berson, S.; Guillerez, S.; Douheret, O.; Ruttens, B.; D'Haen, J.; Adriaensens, P.; Manca, J.; Lutsen, L.; Vanderzande, D. *J. Mater. Chem.* **2009**, *19*, 5424−5435. (e) Szarko, J. M.; Guo, J.; Liang, Y.; Lee, B.; Rolczynski, B. S.; Strzalka, J.; Xu, T.; Loser, S.; Marks, T. J.; Yu, L.; Chen, L. X. *Adv. Mater.* **2010**, *22*, 5468−5472. (f) Yang, L.; Zhou, H.; You, W. *J. Phys. Chem. C* **2010**, *114*, 16793−16800.
(30) Bredas, J. L.; Silbey, R. J. *Conjugated Polymers: the Novel Science and Technology of Highly Conducting and Nonlinear Optically Active Materials*; Kluwer Academic Publishers: Dordrecht, 1991.
(31) (a) Beaujuge, P. M.; Ellinger, S.; Reynolds, J. R. *Adv. Mater.* **2008**, *20*, 2772−2776. (b) Beaujuge, P. M.; Ellinger, S.; Reynolds, J. R. *Nat. Mater.* **2008**, *7*, 795−799. (c) Amb, C. M.; Beaujuge, P. M.; Reynolds, J. R. *Adv. Mater.* **2009**, *22*, 724−728.
(32) Potscavage, W. J.; Sharma, A.; Kippelen, B. *Acc. Chem. Res.* **2009**, *42*, 1758−1767.
(33) Welch, G. C.; Coffin, R.; Peet, J.; Bazan, G. C. *J. Am. Chem. Soc.* **2009**, *131*, 10802−10803.
(34) Lee, J. K.; Ma, W. L.; Brabec, C. J.; Yuen, J.; Moon, J. S.; Kim, J. Y.; Lee, K.; Bazan, G. C.; Heeger, A. J. *J. Am. Chem. Soc.* **2008**, *130*, 3619−3623.
(35) (a) Wienk, M. M.; Kroon, J. M.; Verhees, W. J. H.; Knol, J.; Hummelen, J. C.; Hal, P. A. v.; Janssen, R. A. J. *Angew. Chem., Int. Ed.* **2003**, *42*, 3371−3375. (b) Zhang, F.; Jespersen, K. G.; Björström, C.; Svensson, M.; Andersson, M. R.; Sundström, V.; Magnusson, K.; Moons, E.; Yartsev, A.; Inganäs, O. *Adv. Funct. Mater.* **2006**, *16*, 667−674.
(36) (a) Alvin, M. G.; Albert, R. *J. Appl. Phys.* **1971**, *42*, 2823−2830. (b) Melzer, C.; Koop, E. J.; Mihailetchi, V. D.; Blom, P. W. M. *Adv. Funct. Mater.* **2004**, *14*, 865−870.
(37) Mihailetchi, V. D.; Duren, J. K. J. v.; Blom, P. W. M.; Hummelen, J. C.; Janssen, R. A. J.; Kroon, J. M.; Rispens, M. T.; Verhees, W. J. H.; Wienk, M. M. *Adv. Funct. Mater.* **2003**, *13*, 43−46.
(38) Tanase, C.; Meijer, E. J.; Blom, P. W. M.; de Leeuw, D. M. *Phys. Rev. Lett.* **2003**, *91*, 216601.
(39) Mihailetchi, V. D.; Koster, L. J. A.; Blom, P. W. M.; Melzer, C.; de Boer, B.; van Duren, J. K. J.; Janssen, R. A. J. *Adv. Funct. Mater.* **2005**, *15*, 795−801.